Influence of system size on spatiotemporal dynamics of a model for plastic instability: Projecting low-dimensional and extensive chaos

Article *in* Physical Review E · May 2013

DOI: 10.1103/PhysRevE.87.052907 · Source: PubMed

CITATIONS
9

READS
59

2 authors:

Ritupan Sarmah
Tezpur University
12 PUBLICATIONS **158** CITATIONS

SEE PROFILE

G. Ananthakrishna
Indian Institute of Science
175 PUBLICATIONS **2,757** CITATIONS

SEE PROFILE

Influence of system size on spatiotemporal dynamics of a model for plastic instability: Projecting low-dimensional and extensive chaos

Ritupan Sarmah* and G. Ananthakrishna†
Materials Research Centre, Indian Institute of Science, Bangalore 560012, India
(Received 1 February 2013; published 10 May 2013)

This work is a continuation of our efforts to quantify the irregular scalar stress signals from the Ananthakrishna model for the Portevin–Le Chatelier instability observed under constant strain rate deformation conditions. Stress related to the spatial average of the dislocation activity is a dynamical variable that also determines the time evolution of dislocation densities. We carry out detailed investigations on the nature of spatiotemporal patterns of the model realized in the form of different types of dislocation bands seen in the entire instability domain and establish their connection to the nature of stress serrations. We then characterize the spatiotemporal dynamics of the model equations by computing the Lyapunov dimension as a function of the drive parameter. The latter scales with the system size only for low strain rates, where isolated dislocation bands are seen, and at high strain rates, where fully propagating bands are seen. At intermediate applied strain rates corresponding to the partially propagating bands, the Lyapunov dimension exhibits two distinct slopes, one for small system sizes and another for large. This feature is rationalized by demonstrating that the spatiotemporal patterns for small system sizes are altered from the partially propagating band types to isolated burst type. This in turn allows us to reconfirm that low-dimensional chaos is projected from the stress signals as long as there is a one-to-one correspondence between the bursts of dislocation bands and the stress drops. We then show that the stress signals in the regime of partially to fully propagative bands have features of extensive chaos by calculating the correlation dimension density. We also show that the correlation dimension density also depends on the system size. A number of issues related to the system size dependence of the Lyapunov dimension density and the correlation dimension density are discussed.

DOI: 10.1103/PhysRevE.87.052907 PACS number(s): 05.45.Tp

I. INTRODUCTION

Many physical, chemical, and biological experimental systems exhibit irregular signals. There is a large body of literature devoted to determining whether these signals are of deterministic origin or stochastic origin and designing algorithms to filter the inevitable noise component and then analyze the resulting signal. These methods work as long as the dimension of the attractor is low. However, much less attention has been paid to quantifying irregular signals that cannot be classified as low-dimensional (low-d) chaos. This question is particularly important since one often measures output signals of spatially extended systems. In such cases, while the internal degrees of freedom are not accessible to experiments, they are suspected to be spatiotemporally chaotic, a view supported by models that capture the basic features of the phenomenon. Indeed, such scalar output signals, which are some kind of spatial average over the internal degrees of freedom of spatially extended systems, are easy to generate from model systems. A concrete example is the plastic deformation of metallic alloys subjected to a constant strain rate test. In this case, only stress can be measured by the load cell placed at one end of the sample and is the spatial average of dislocation activity in the entire sample. Moreover, stress is also a dynamical variable that controls the spatial activity of the internal degrees of freedom. Under normal conditions, the conventional yield phenomenon is observed with the stress smoothly changing over from the linear elastic limit to nonlinear plastic flow even though dislocation motion is known to be intermittent at the microscopic level [1,2]. The latter is indeed evident in the intermittent bursts of acoustic emission signals observed during the normal yield process [3]. (Actually, the intermittent flow is almost the rule when sample sizes are of micrometer dimensions [2,4–7].) Simulations also suggest the intermittent motion [8,9]. However, when specimens of dilute metallic alloys are deformed in a certain window of strain rates and temperatures, the measured stress signals $\sigma(t)$ are irregular and are referred to as serrations in the metallurgical literature. These serrations are attributed to collective pinning and unpinning of dislocations from solute atmosphere. The phenomenon is known as the Portevin–Le Chatelier (PLC) effect [1,10,11]. These serrations are associated with heterogeneous deformation [1,11]. While dislocation activity in the sample is not accessible to experiments, dislocation bands seen on the surface of the sample [1,12] together with the nature of accompanying acoustic emission signals [13,14] strongly suggest that the collective dislocation dynamics is intermittent at the microscopic level. The nature of the stress signals while remaining irregular throughout the instability domain changes with the applied strain rate. Furthermore, the qualitative features of the stress signals such as the amplitude and the mean periodicity have been correlated with the types of dislocation bands seen on the surface of the sample. Such experimental stress signals (in single and polycrystals) have been analyzed and two types of dynamics have been detected [15–18]. While low-d chaos has been reported at low strain rates, scale-free power law distributions of stress-drop magnitudes have been reported at high strain rates [16–18]. The fact that

*ritupan@mrc.iisc.ernet.in
†garani@mrc.iisc.ernet.in

the fluctuating stress-time series at low strain rates has features of low-d chaos suggests the possibility of projecting low-d chaos from spatiotemporal dynamics. In contrast, the power law distribution of magnitudes of the stress drops at high drive rates suggests high-dimensional dynamics and possibly extensive chaos. Thus it appears that the nature of irregular stress serrations may exhibit different types of dynamics in different regimes of drive rates.

A second example is the crackling audible noise, called acoustic emission (AE), commonly experienced during peeling of adhesive tape [19–23]. Again experimental acoustic emission signals are found to be irregular over a range of pull velocities [20,22,23]. The nature of the peel front is found to be fibrillar [24,25]. A model for the peel front dynamics shows that the nature of the AE signals is determined by the spatial average of the local slip rates of the rugged fibrillar nature of the peel front [21–23]. The experimental AE signals have been analyzed and have been shown to be low-d chaotic in a subinterval of pull velocities where the AE signals are irregular [21,22]. Here again a power law distribution of AE signal amplitudes has also been detected [22,23], an indication of high-dimensional chaos. This may again suggest two distinct types of dynamics in different regimes of forcing. Model AE signals have also been shown to have features of low-d chaos. A power law distribution of model AE signal amplitudes has also been detected [21–23]. Several other examples studied in the literature fall into this category where the scalar time series is the average of spatial degrees of freedom such as the electrocardiogram data [26], the mean rainfall over a certain localized region [27], and the position and intensity of a light beam passing through a turbulent medium [28], to cite a few.

The above examples suggest the possibility that the process of spatial averaging of the internal degrees of freedom may project low-d chaos and possibly high-dimensional or extensive chaos in different regimes of forcing. Recently, using the Ananthakrishna (AK) model for the PLC effect, we demonstrated that the stress signal, which is directly related to the spatial average of dislocation activity in the entire sample, could be unambiguously identified as having all features of low-d chaos while the full set of equations was spatiotemporally chaotic [29]. We further showed that this was entirely due to the one-to-one correspondence between the randomly nucleated isolated bursts of mobile dislocation density (or, equivalently, dislocation bands) and the stress drops. We supported the numerical results by demonstrating that the full set of model equations can be approximately reduced to space-independent model equations for the space-averaged dislocation densities. These reduced equations have the same form as the space-independent (bare) AK model, which is known to be low-dimensionally chaotic. However, the scaling regime for the correlation dimension shrinks with increasing applied strain rate due to the increasing propensity for propagation of the dislocation bands. Thus the irregular stress signals corresponding to the substantial regime of strain rates of the instability remained unquantified. Here we propose to quantify the irregular stress-times series in the region of applied strain rates where partially propagating to fully propagating bands are seen.

As in the previous investigation, hereafter referred to as I [29], we use the AK model for the PLC effect. We first elucidate the relationship between the spatiotemporal patterns (dislocation band types) of the model and the nature of stress serrations. The model reproduces the three experimentally observed dislocation bands, namely, the uncorrelated type C, partially propagating (hopping) type B, and the fully propagating type A found with increasing applied strain rate. We also quantify the spatiotemporal dynamics of the model by calculating the number of positive Lyapunov exponents and the Lyapunov dimension as a function of the system size for the entire range of applied strain rates of the instability. In the range of strain rates of interest corresponding to the partially propagating regime, the Lyapunov dimension exhibits two distinct slopes as a function of the system size, one for small values and another for large. The underlying reason for this feature is traced to the fact that the nature of spatiotemporal patterns is sensitive to the system size. Specifically, well separated bands are seen for small system sizes in the region of strain rates where partially propagative bands are seen for large system sizes (say $N = 100$). This property is used to reconfirm that low-d chaos is projected as long as the one-to-one correspondence between the isolated bursts of mobile dislocation density and the stress drops remains valid, as is the case for the randomly nucleated isolated bands [29]. In this regime of strain rates corresponding to the partially to fully propagating bands, we show the existence of the correlation dimension density. We also show that the magnitude of the correlation dimension density is affected when the system size is small in the fully propagative band regime. We conclude the paper by discussing several questions raised by our study.

II. THE PORTEVIN–LE CHATELIER EFFECT

We begin by briefly summarizing the relevant generic features of the PLC effect with a view to provide the physical basis for the AK model. The PLC instability manifests itself as irregular stress-time signals when samples of dilute alloys are deformed under constant strain rate conditions. The instability is seen only in a window of strain rates and temperatures. Each stress drop of the intermittent flow is associated with the formation and often the propagation of dislocation bands. Three distinct types of dislocation bands and the associated serrations have been identified. At low strain rates (or high temperature) randomly nucleating uncorrelated static bands called type C are seen. The associated stress serrations consist of nearly regular large-amplitude stress drops. At intermediate strain rates, spatially correlated "hopping" type-B bands with smaller stress drops are seen. At high strain rates, propagating type-A bands with numerous small-amplitude stress drops are observed.

The classical explanation due to Cottrell envisages a dynamic interaction between mobile dislocations and diffusing solute atoms [1,11]. The approach was later extended by others [30–32]. At low strain rates (or high temperatures) the average velocity of dislocations is low and there is sufficient time for the solute atoms to diffuse to the dislocations and pin them (called aging). Thus the longer the dislocations are arrested (determined by the time scale of the applied strain rate), the larger will be the stress required to unpin them. When these dislocations are unpinned, they move at high speeds until they are arrested again. The characteristic large stress

drop observed at low strain rates is due to the sufficient time available for the solute atoms to reach a near-saturation level at the cores of dislocations. Stress-strain curves in this regime have typical features of relaxational oscillations. At higher strain rates, the time available for solute atoms to diffuse to the dislocations decreases and hence the stress required to unpin them decreases. Thus the PLC instability manifests in a range of strain rates and temperatures where these two time scales are of the same order of magnitude. Much of the above explanation has remained hand-waving, which, as we will see, will be made quantitative.

However, relating the irregular stress signal to the underlying dislocation dynamics has remained a difficult task for a long time due to the absence of dislocation-based models. A simple calculation of the order of magnitude of stress drops shows that a large number of dislocations need to be pinned and unpinned simultaneously, i.e., some kind of cooperative behavior needs to be built up starting from the initial random configurations of dislocations. However, understanding the collective behavior of dislocations has been slow largely due to the lack of techniques describing the cooperative behavior of dislocations. Since the AK model for the PLC effect uses a dynamical approach, it serves as a convenient model for investigating the spatiotemporal patterns and their connection to the stress serrations.

Several generic features of the PLC effect such as the existence of the instability within a window of strain rates and temperature and negative strain rate sensitivity of the flow stress are captured by the bare AK model (which excludes the spatial degrees of freedom) [1,33]. One prediction that is specific to the model is that stress drops could be chaotic at low strain rates [34]. The prediction has been subsequently verified using experimental signals from single and polycrystals [15–18]. Further analysis of experimental stress-strain curves at high strain rates showed a power law distribution of stress-drop magnitudes [16–18]. An extension of the model to include spatial degrees of freedom not only predicts the different types of bands and the associated stress serrations [1,35–37], but also recovers the power law distribution of stress-drop magnitudes observed at high strain rates corresponding to the propagating type-A bands.

III. THE ANANTHAKRISHNA MODEL

The AK model attributes most generic features of the PLC effect to the nonlinear interaction of a few dislocation populations assumed to represent the collective degrees of freedom of the system [33,35–37]. The well separated time scales subsumed in the dynamic interaction of dislocations with solute atoms are captured by the three types of dislocations, namely, the fast mobile ρ_m, immobile ρ_{im}, and the "decorated" Cottrell-type dislocations ρ_c. Here again we ignore the strain hardening term as was done in I [29] (due its irrelevance to dynamical properties); the scaled form of the evolution equations are

$$\frac{\partial \rho_m}{\partial t} = -b_0\rho_m^2 - \rho_m\rho_{im} + \rho_{im} - a\rho_m + \phi^m\rho_m + \frac{D\phi^m(t)}{\rho_{im}}\frac{\partial^2\rho_m}{\partial x^2}, \tag{1}$$

$$\frac{\partial \rho_{im}}{\partial t} = b_0\left(b_0\rho_m^2 - \rho_m\rho_{im} - \rho_{im} + a\rho_c\right), \tag{2}$$

$$\frac{\partial \rho_c}{\partial t} = c(\rho_m - \rho_c), \tag{3}$$

$$\frac{d\phi(t)}{dt} = d\left[\dot{\epsilon}_a - \frac{\phi^m(t)}{l}\int_0^l \rho_m(x,t)dx\right] = d[\dot{\epsilon_a} - \dot{\epsilon}_p(t)]. \tag{4}$$

The model includes the following dislocation mechanisms: immobilization of two mobile dislocations due to the formation of locks ($b_0\rho_m^2$), the annihilation of a mobile dislocation with an immobile one ($\rho_m\rho_{im}$), and the remobilization of the immobile dislocation due to stress or thermal activation (ρ_{im}). It also includes the immobilization of mobile dislocations due to solute atoms ($a\rho_m$). Once a mobile dislocation starts acquiring solute atoms, it is regarded as the Cottrell-type dislocation ρ_c. As the dislocations progressively acquire more solute atoms, they eventually stop, at which point they are considered as immobile dislocations ρ_c defined by $\rho_c = \int_{-\infty}^{t} dt'\rho_m(t')K(t-t')$, where $K(t)$ is an appropriate kernel. For the sake of simplicity, this kernel is modeled using a single time scale $K(t) = e^{-ct}$. The fifth term in Eq. (1) represents the rate of multiplication of dislocations due to cross-slip. This depends on the velocity of the mobile dislocations represented by $V_m(\phi) = \phi^m$, where ϕ is the scaled stress and m the velocity exponent. In terms of unscaled stress σ, $\phi = \frac{\sigma}{\sigma_y}$, where σ_y is the yield stress. The diffusive spatial coupling in Eq. (1) arises due to a cross-slip mechanism that allows dislocations to spread into neighboring spatial locations. These equations are coupled to the machine equation (4), which represents the constant strain rate deformation experiment. The applied strain rate in unscaled units is $\dot{\varepsilon}_a = \frac{d}{dt}\frac{dL}{L}$, where L is the length of the sample. (The PLC instability is found in the range of strain rates from 10^{-6} to 10^{-3} s^{-1}.) In Eq. (4), $\dot{\epsilon}_a$ is the dimensionless applied strain rate ($\dot{\epsilon}_a = \frac{d}{d\tau}\frac{dl}{l}$, where τ is the dimensionless time and l the dimensionless length of the sample) and d the scaled effective compliance of the machine and the sample. The scaled constants a, b_0, and c refer, respectively, to the concentration of solute atoms slowing down the mobile dislocation, the thermal and athermal reactivation of immobile dislocations, and the diffusion rate of solute atoms around the mobile dislocations.

The numerical solutions of the Eqs. (1)–(4) are carried out on a grid of N points by taking the scaled length of the sample $l = N\Delta X$, where ΔX is the unit grid length. We used an adaptive step size differential equation solver (MATLAB ode23), keeping ΔX fixed so that N represents the size of the system. The physically relevant parameter is the applied strain rate $\dot{\epsilon}_a$ with respect to which different types of bands and the associated serrations are observed. The instability range is found in the interval $20 \leqslant \dot{\epsilon}_a < 1650$ when the system size is $N = 100$. It must be mentioned that the instability limit of a single oscillator (i.e., the bare AK model) is 3–300. The instability is suppressed when the system size is small, say, less than 10, even though the bare model remains unstable in the region. This already suggests the influence of the system size on the spatiotemporal dynamics.

In our model, the spatial dependence of ρ_{im} and ρ_c arises only through ρ_m. For our numerical calculations, we use

the initial values of the densities along the sample drawn from a uniform Gaussian distribution with a finite spread. However, since the long-term evolution does not depend on the initial values, the steady state values are used. The physical condition that bands cannot propagate into the grips requires the boundary values $\rho_{im}(1,t)$ and $\rho_{im}(N,t)$ be two orders higher than $\rho_{im}(j)$, $j = 2,\ldots,N-1$. Furthermore, we impose $\rho_m(j,t) = \rho_c(j,t) = 0$ for $j = 1$ and N. The results reported are for $a = 0.8$, $b = 5 \times 10^{-4}$, $c = 0.08$, $d = 6 \times 10^{-5}$, $m = 3$, and $D = 0.25$. Stress $\phi(t)$ is sampled at time intervals $\delta t = 0.5$ by interpolating the original data after discarding the initial transients of 20 000 points.

IV. SPATIOTEMPORAL PATTERNS AND ASSOCIATED STRESS SERRATIONS

Since the stress is a scalar dynamical variable related to the spatial average of dislocation activity in the entire sample, it does influence the spatiotemporal patterns. To understand this, we begin by discussing the basic instability mechanism operating in the model by examining Eqs. (1) and (4). From Eq. (1) it is clear that ρ_m increases abruptly only when ϕ exceeds unity (corresponding to the unscaled stress σ exceeding the yield stress σ_y). Equivalently, there is a threshold for nucleation of an isolated burst of mobile density ρ_m identified with an isolated dislocation band. However, a stress drop can only occur when the space-averaged plastic strain rate $\dot{\epsilon}_p = \frac{\phi^m(t)}{l}\int_0^l \rho_m(x,t)dx$ exceeds the applied strain rate $\dot{\epsilon}_a$. Thus the scalar stress at a given time controls the production of dislocations, which in turn controls the stress.

As shown in I [29], the model reproduces all three types of bands (C, B, and A) observed in experiments with increasing strain rate. While the metallurgical literature identifies the three band types and the associated stress-strain curves, there is no clear understanding of the evolution of bands with increasing $\dot{\epsilon}_a$. In the AK model, for a range of low $\dot{\epsilon}_a$, we find the static uncorrelated type-C bands [1,29,37]. As we increase $\dot{\epsilon}_a$, we find the hopping type-B bands. The stress-strain curves are more irregular with average amplitude smaller than that for the type-C bands. At high strain rates, the continuously propagating type-A bands are seen. The corresponding stress-time series is very irregular with mostly small-amplitude stress drops. While the fact that the AK model predicts the three types of bands has been known for some time [1,37], whether these distinct band types are due to successive bifurcations or whether the changes are continuous has not been addressed. Furthermore, one does not know what dynamical changes lead to these distinct spatiotemporal patterns. From a dynamical point of view, what is required is a clear understanding of the cause-effect relationship between the changes in the spatiotemporal pattern and the associated stress fluctuations. In what follows, we attempt to elucidate the influence of $\dot{\epsilon}_a$ on the spatiotemporal patterns (or, equivalently, the nature of dislocation bands) and its connection to the nature of the stress-time series. While this aspect was dealt with briefly in I [29], it will be investigated in some detail as this is particularly important for understanding the nature of the dynamics projected from stress signals.

In what follows, the spatiotemporal patterns discussed are for a system size $N = 100$. (This size is large enough that the spatiotemporal patterns are not affected by a further increase in the system size.) At the lower end of the instability, from $\dot{\epsilon}_a =$ 20 to 50, randomly nucleated dislocation bands corresponding to isolated bursts of ρ_m are seen. From the above discussion we know that such a burst of ρ_m can only be nucleated if the scaled stress ϕ increases beyond unity. A typical space-time plot of randomly nucleated bands is shown in Fig. 1(a) for $\dot{\epsilon}_a =$ 40. The corresponding stress-strain curve is nearly regular, as illustrated in Fig. 1(b). Furthermore, in this range of $\dot{\epsilon}_a$, usually a single burst of ρ_m contributes to the total plastic strain rate $\dot{\epsilon}_p = \frac{\phi^m(t)}{l}\int_0^l \rho_m(x,t)dx$ as the magnitude of $\rho_m(x,t)$ at other spatial locations is insignificant. This implies that whenever the space-averaged plastic strain rate $\dot{\epsilon}_p(t)$ overshoots the applied strain rate $\dot{\epsilon}_a$, a stress drop occurs [see Eq. (4)]. Thus there is a one-to-one correspondence between bursts of mobile density ρ_m and the stress drops. However, occasionally, one does find a few low-amplitude stress drops. This can be traced to the superposition of slightly out-of-phase contributions from two spatially well separated bursts of $\rho_m(x,t)$ to the space-averaged plastic strain rate $\dot{\epsilon}_p(t)$. To illustrate this we have displayed another segment of the space-time plot of $\rho_m(x,t)$ in Fig. 2(a). The arrows in Figs. 2(a) and 2(b) show the correspondence between the two bursts of ρ_m and the small-amplitude stress drops.

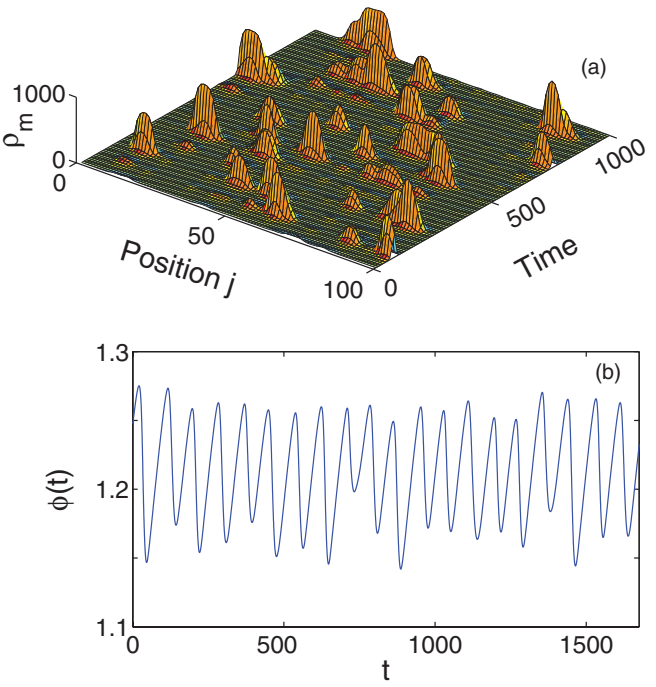

FIG. 1. (Color online) (a) Randomly nucleated type-C bands for $\dot{\epsilon}_a = 40$ and $N = 100$. (b) The corresponding stress-time plot.

The extent of spatial correlation between the bursts of ρ_m at low $\dot{\epsilon}_a$ can be attributed to the interplay of two factors. First, recall that a burst of mobile dislocation density ρ_m can only occur when the stress exceeds unity. Once such a burst of ρ_m is created, at low strain rates, there is enough time for the dislocation burst to die off completely before another one is nucleated. The second factor is that the mean period of the stress serrations is proportional to the inverse of the

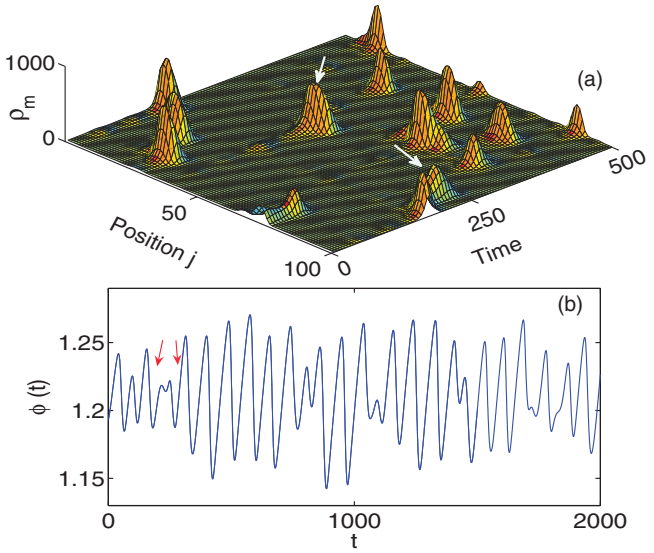

FIG. 2. (Color online) (a) Another segment of the space-time plot of randomly nucleating type-C bands for $\dot{\epsilon}_a = 40$. Two slightly off-phase mobile density bursts are shown. (b) The resulting stress-time curve. The small stress drops shown between the arrows in (b) arise from the superposition of the two out-of-phase ρ_m bursts shown by two arrows. A shorter segment of space-time plot is shown for the sake of identification of the small stress drop.

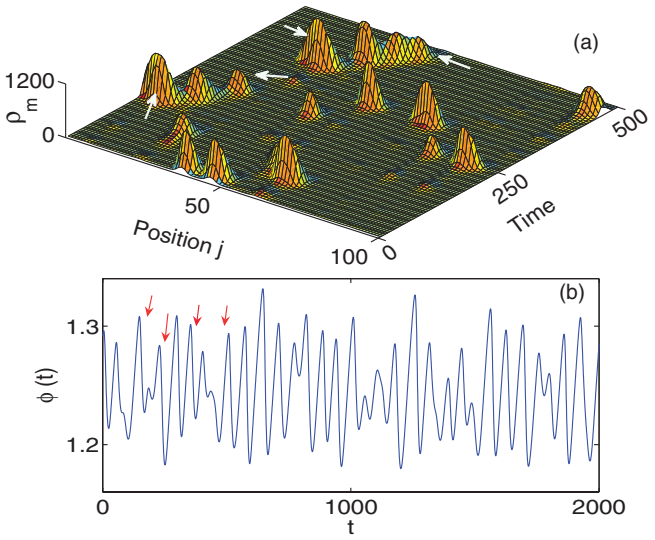

FIG. 3. (Color online) (a) Early stages of partially propagating bands for $\dot{\epsilon}_a = 60$. (b) The corresponding stress-time plot. The small stress drops shown between the two sets of arrows in (b) correspond to the two hopping partially propagating bands between $j = 1$–18 and 12–46, respectively, shown by the two sets of arrows in (a). A shorter segment of the space-time plot is shown for the sake of identification of small stress drops.

applied strain rate. Thus the mean period of the serrations decreases with increasing $\dot{\epsilon}_a$. Then increasing $\dot{\epsilon}_a$ leaves less time for a dislocation burst to be completed and hence it is more favorable to nucleate another burst of ρ_m just ahead of it before the previous burst has died out completely since during this time interval, the stress would have relaxed only partially as the space-averaged plastic strain rate $\dot{\epsilon}_p(t)$ still remains larger than $\dot{\epsilon}_a$. This in turn implies that the stress required to induce a new burst ahead of the previous one is less than that required to nucleate an isolated dislocation burst elsewhere. For the same reason, even the smallest extent of propagation introduces a short segment of small-amplitude stress drops in the otherwise long stretches of large-amplitude drops. Such propagative events increase with increasing strain rate to accommodate the decreasing period. Concomitantly, the segments of small-amplitude serrations increase with $\dot{\epsilon}_a$. The net result is that the average stress-drop magnitude decreases with increasing $\dot{\epsilon}_a$. The nucleation of a band ahead of the previous one gives the visual impression of hopping-type partial propagation (type-B band). Such hopping-type propagative events are noticeable even at $\dot{\epsilon}_a = 60$. A plot of $\rho_m(x,t)$ for $\dot{\epsilon}_a = 60$ is shown in Fig. 3(a). Note that in this case, the second burst of ρ_m appears when the first one has almost vanished. The associated stress-time curve is shown in Fig. 3(b). The small stress drops shown between the two sets of arrows in Fig. 3(b) correspond to the two hopping type of propagating bands between $j = 1$–22 and 18–46, respectively, shown by the two sets of arrows in Fig. 3(a). With a further increase in $\dot{\epsilon}_a$, the tendency for the formation of a new burst of ρ_m ahead of the previous ρ_m burst increases, giving the impression of hopping character and therefore identified with the type-B band. A plot of the partially propagating type-B band is shown in Fig. 4(a) for $\dot{\epsilon}_a = 90$. The corresponding stress-strain curve is considerably more irregular with small stretches of small-amplitude stress drops separating the large

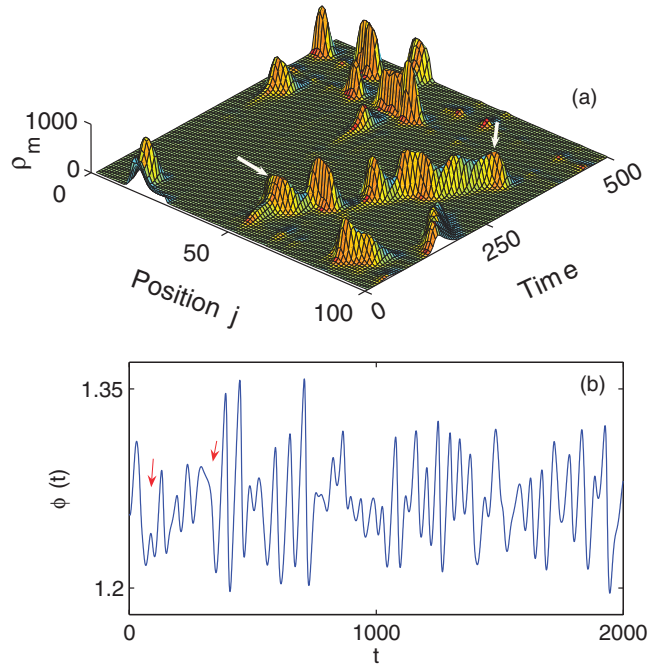

FIG. 4. (Color online) (a) Partially propagating (hopping type-B) bands for $\dot{\epsilon}_a = 90$. (b) The corresponding stress-time plot. The correspondence between the propagating nature of the band marked by the arrows in (a) and the stress-time series in (b) is displayed.

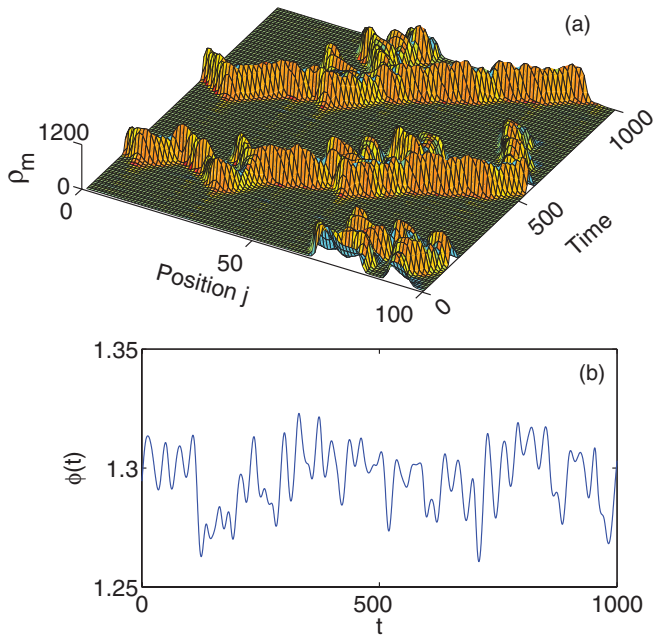

FIG. 5. (Color online) (a) Continuously propagating bands for $\dot{\epsilon}_a = 240$. (b) The corresponding stress-time plot.

stress drops. Note also that a large stress drop can only be seen after ρ_m has nearly vanished followed by the nucleation of a burst of ρ_m. With a further increase in $\dot{\epsilon}_a$, the separation in time and space between successive bursts of ρ_m is not even noticeable. Note that at high $\dot{\epsilon}_a$, the instantaneous value of the stress would be such that $\dot{\phi}(t)$ has just turned negative before another burst is created. This also implies that a new burst is created just after the burst has marginally dropped from its peak value, leading to an increased level spatial correlation to such an extent that the bands propagate fully. This kind of fully propagating band is identified with the type-A band in the literature. The corresponding serrations have numerous small-amplitude stress drops with a few large-amplitude drops [1,37]. The latter can be identified with the band reaching the edge of the sample (in both the model and experiments). A typical plot of the fully propagating band (type A) is shown in Fig. 5(a) with some interruptions and distortions, as can be seen from the figure. The corresponding stress-time plot is shown in Fig. 5(b). Undistorted solitary wavelike solutions are rare, but not impossible to find. (For example, one such plot has been shown in Fig. 65 of Ref. [1].) For the fully propagative bands, we have demonstrated earlier that Eqs. (1)–(4) can be reduced to the Fisher-Kolmogorov equation for the fast variable $\rho_m(x,t)$ by projecting the full dynamics onto the fast manifold (see Ref. [1], p. 224). This then permits us to obtain an analytical expression for the velocity of the propagative wave using the marginal stability hypothesis [1,38]. However, we do not find solitonlike solutions that after interacting remain unaffected once the two solitary waves move beyond the range of interaction. Indeed, distortions arise as bands can be nucleated at other spatial locations or there could be reflections at the end of the specimen. From the above discussion, the succession of small stress drops can be taken to be the signature of the extent of spatial correlation. The discussion also points to the presence of two length scales, one corresponding to the mean width l_b of the bursts of ρ_m and another to the extent of propagation l_p.

For the sake of completeness, and in view of the fact that the model reproduces the three types of bands reported in experiments, we briefly compare the model stress-time curves with those from experiments for a few strain rate values. Since the stress signals are directly related to the spatial average over the dislocation activity in the entire sample, a proper comparison would be in terms of statistical and dynamical properties. [Such a comparison has been reported elsewhere (see Refs. [1,35]).] Figures 6(a) and 6(b) show two stress-time curves for low ($\dot{\epsilon}_a = 3.3 \times 10^{-6}$ s^{-1}) and high ($\dot{\epsilon}_a = 8.3 \times 10^{-5}$ s^{-1}) strain rates, respectively, obtained from the deformation of samples of Cu10%Al alloy. Despite the fact that these two time series have significantly sharper upturns from those of the model time series [Fig. 1(b) and Fig. 5(b)], some average features such as the mean amplitude compare well [39]. First consider comparing the model stress signal at low strain rates in Fig. 1(b) (type-C bands) with the low strain rate experimental signal in Fig. 6(a). It is clear that both stress signals exhibit mostly large-amplitude stress drops. In contrast, the model stress signals in Fig. 5(b) corresponding to $\dot{\epsilon}_a = 240$ (type-A propagating band) and the experimental stress signals in Fig. 6(b) have numerous small-amplitude stress drops with very few large stress drops. Indeed, over the small stretch presented, it is clear that the amplitude ratio between the low and high strain rate model and experimental time series decrease approximately by a factor of $\frac{1}{2}$.

The distribution of the stress-drop magnitudes (the difference between a maximum and the following minimum) corresponding to the experimental stress-time series $D(\Delta\sigma)$

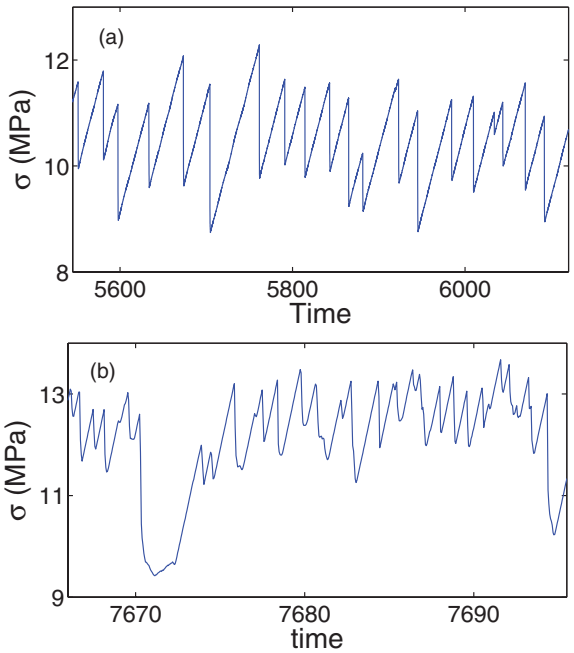

FIG. 6. (Color online) Stress-strain series from the deformation of Cu10%Al alloy samples for strain rates of (a) 3.3×10^{-6} s^{-1} and (b) 8.3×10^{-5} s^{-1}.

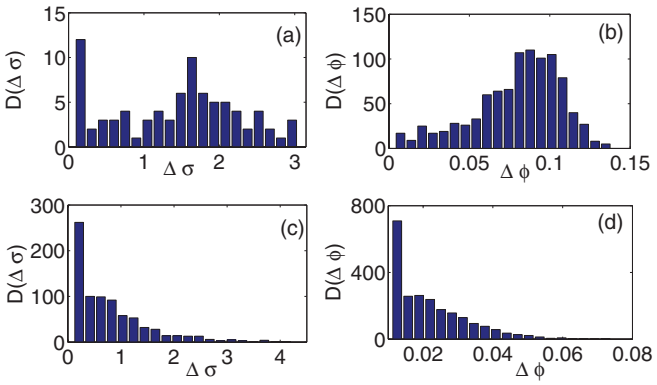

FIG. 7. (Color online) Distribution of stress drop magnitudes for experimental and model time series: (a) $D(\Delta\sigma)$ for the experimental stress-time series for a strain rate of 3.3×10^{-6} s^{-1}, (b) $D(\Delta\phi)$ for the model stress-time series for $\dot{\epsilon}_a = 40$, (c) $D(\Delta\sigma)$ for the experimental stress-time series for a strain rate of 8.3×10^{-5} s^{-1}, and (d) $D(\Delta\phi)$ for the model stress-time series for $\dot{\epsilon}_a = 240$.

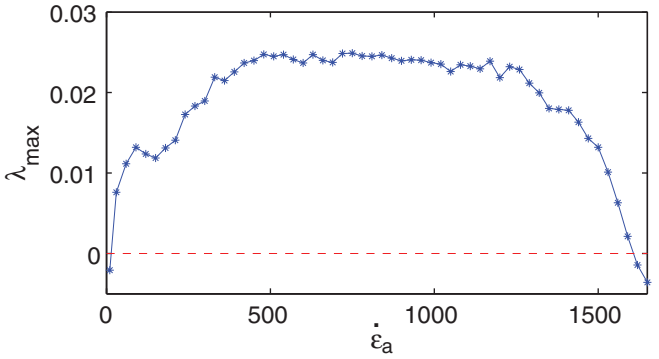

FIG. 8. (Color online) Plot of the largest Lyapunov exponent for $N = 100$ as a function of $\dot{\epsilon}_a$.

[Fig. 6(b)] and that of the model $D(\Delta\phi)$ for low strain rates [Fig. 1(b)] show a peaked nature, as is clear from Figs. 7(a) and 7(b). The sharp peak at the lower end of $D(\Delta\sigma)$ in Fig. 7(a) for the experimental signal can be attributed to fluctuations at small scales due to the machine inaccuracy. The peaked nature of the distribution is a generic feature of stress signals from most low strain rate cases (see Fig. 4 of Ref. [18]). As the applied strain rate is increased, the distributions for experimental and model signals develop increasing skewness to the right. Eventually, at high strain rates corresponding to type-*A* propagating bands, the distributions of stress-drop magnitudes show long tails starting from peaks located at small values. The corresponding distributions for the experimental and model time series are shown in Figs. 7(c) and 7(d), respectively. When these distributions are plotted on a log-log scale, we find that they follow a power law with an exponent value close to -1.1 (see Fig. 2 of Ref. [35], where a log-log plot is shown). Finally, it must be stated that the reconstructed attractor from the low strain rate experimental time series using the first three principle components (obtained from singular value decomposition) look quite similar to the model attractor for an arbitrary site (see Fig. 2 of Ref. [35]).

V. SPATIOTEMPORAL DYNAMICS OF THE MODEL

We first consider characterizing the spatiotemporal dynamics of the model. Towards this end, the spectrum of Lyapunov exponents for the model equations (1)–(4) has been calculated using the standard method due to Benettin *et al.* [40].

Three different types of calculations have been carried out. Unlike most reports in the literature, the dynamical invariants such as the Lyapunov dimension or Kolmogorov-Sinai entropy depend on the system size, as we show below. Even though the largest Lyapunov exponent $\lambda_{\max}$ also depends on the system size, for purposes of locating the instability domain, we shall use a system size $N = 100$, which is large enough to be regarded as a large system size. The instability domain is found to be $20 < \dot{\epsilon}_a \leqslant 1625$. A plot of the largest Lyapunov exponent for $N = 100$ is shown in Fig. 8.

However, as stated, $\lambda_{\max}$ also depends on the system size. The minimum system size $N_{\min}$ for which the system is spatiotemporally chaotic also depends on $\dot{\epsilon}_a$. At the lower end of the instability $N_{\min}$ is large. For instance, for $\dot{\epsilon}_a = 25$, $N_{\min} = 45$. However, $N_{\min}$ decreases rapidly as we increase $\dot{\epsilon}_a$. For instance, even for $\dot{\epsilon}_a = 40$, $N_{\min} \sim 15$, and beyond $\dot{\epsilon}_a = 60$, $N_{\min}$ drops to about 11, staying constant around 9 for higher values of $\dot{\epsilon}_a$. Note that the value of $\dot{\epsilon}_a$ at which the partial propagation of dislocation bands are seen is $\dot{\epsilon}_a = 60$. The fact that $N_{\min}$ is large at the lower end of the instability can be appreciated by noting that at low $\dot{\epsilon}_a$, only a single dislocation burst is nucleated at any given instant of time.

We have studied the system size dependence of the number of positive exponents n_λ^+, the Lyapunov dimension D_L, and Kolmogorov-Sinai entropy H for a range of values of the system size $N_{\min} \leqslant N \leqslant 150$. We begin with the results on the Lyapunov dimension D_L since the dependence on the system size can be seen unambiguously. As reported in I [29], for low strain rates where isolated bursts of ρ_m are seen at any given time and in the region of fully propagating bands at high $\dot{\epsilon}_a$, D_L scales with the system size with a slope close to 0.37. [See Figs. 4(a) and 4(b) of I [29].] However, in the midregion of $\dot{\epsilon}_a$ where the partially propagating bands are seen ($50 < \dot{\epsilon}_a < 220$), two distinct slopes can be easily detected. (The range of values of N from $N_{\min}$ to $N = 150$ is adequate for this purpose.) Even for $\dot{\epsilon}_a = 60$, where the extent of propagation is small, the change in slope (occurring at $N = 56$ from 0.53 to 0.31) is easily noticeable. As $\dot{\epsilon}_a$ is increased, the larger slope is limited to smaller N values. The magnitudes of the two slopes and the N value at which the slope changes depend on $\dot{\epsilon}_a$. For instance, as we increase $\dot{\epsilon}_a$ to 90, the slope change occurs at $N = 40$. A typical such plot of D_L versus N is shown for $\dot{\epsilon}_a = 150$ in Fig. 9. It is clear that there are two slopes, one for $N \leqslant 30$ with a slope $\sim$0.7 and another for $N \geqslant 30$ with a slope $\sim$0.31. As we increase $\dot{\epsilon}_a$, the value of N at which the slope change occurs gets smaller and eventually one finds only a single slope with a value $\sim$0.37. The value of $\dot{\epsilon}_a$ at which we find a single slope can be identified with the fully propagative band regime.

The underlying cause for the two distinct slopes can be understood by examining the space-time plots for various system sizes. Indeed, we find that for small system sizes, the nature of spatiotemporal patterns is affected due to finite

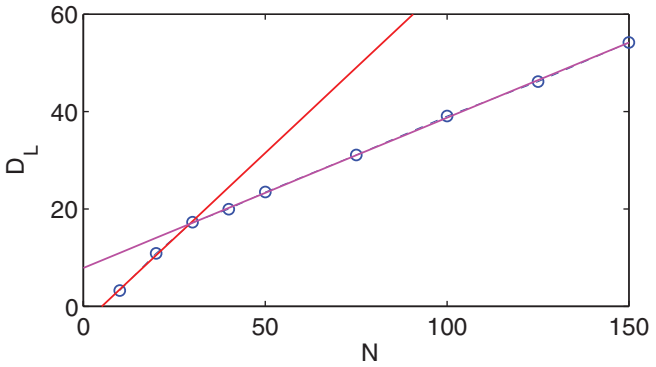

FIG. 9. (Color online) Lyapunov dimension D_L as a function of N for $\dot{\epsilon}_a = 150$. Note the two distinct slopes.

system size. More specifically, keeping the $\dot{\epsilon}_a$ value fixed at a value where the partially propagative bands are seen for a large system size $N = 100$, we find that the spatial patterns are significantly altered when the system size is reduced to small values. For instance, for $\dot{\epsilon}_a = 120$, we find the partially propagative bands for $N = 100$. Keeping $\dot{\epsilon}_a = 120$ and using a small N value, say, $N = 20$, however, changes the partially propagating character to burst-type spatiotemporal pattern. The bursts in ρ_m are well separated in space and time. Even though these bursts are well separated in time, each burst is followed by another burst ahead of it instead of the hopping-type partially propagating bands seen for $N = 100$. (Recall that for $N = 100$ and $\dot{\epsilon}_a = 120$, successive bursts have considerable overlap in space and time, quite unlike for the $N = 20$ case.) A space-time plot for $\rho_m(j,t)$ is shown in Fig. 10(a). Moreover, since only a single burst contributes to the plastic strain rate $\dot{\epsilon}_p(t)$ at any given time, the stress-time plot is nearly regular with mostly large-amplitude stress drops, as can be seen from Fig. 10(b), a feature that is usually seen

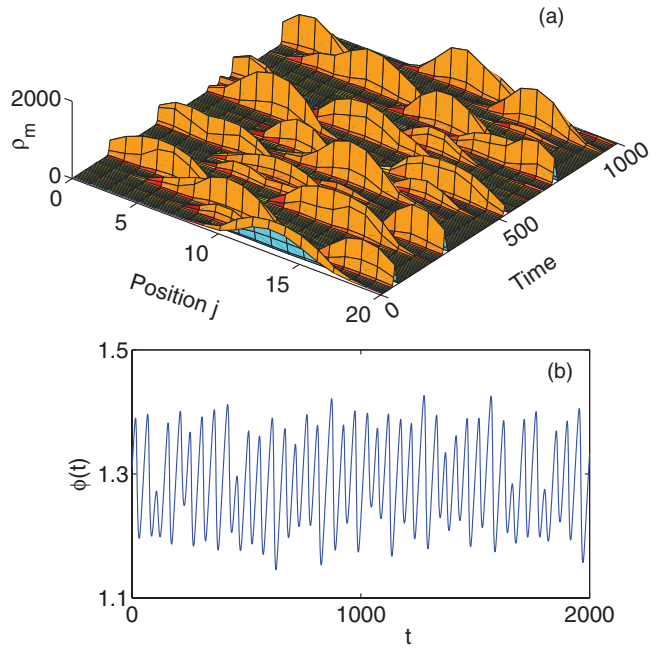

FIG. 10. (Color online) (a) Space-time plot of the mobile dislocation density for $\dot{\epsilon}_a = 120$ and $N = 20$. (b) The corresponding stress-time plot.

for low $\dot{\epsilon}_a$ and large N [compare with Fig. 1(b)]. The only difference in the nature of stress-time plots for $\dot{\epsilon}_a = 120, N = 20$ [Fig. 10(b)] and that for $\dot{\epsilon}_a = 40, N = 100$ [Fig. 1(b)] is that the mean period has decreased. Similar behavior is seen for all values of $\dot{\epsilon}_a$ in the hopping-type propagative regime. This change in the spatial pattern for small system sizes can be attributed to the fact that the length scale corresponding to the spatial extent of the band l_b (typically 12–15 in this case) is comparable to the length scale of propagation l_p. Thus, at any given time only a single burst can be accommodated in a system size of $N = 20$. Thus finite boundary appears to influence the spatiotemporal dynamics when the system size is small and when $\dot{\epsilon}_a$ is in the propagative regime. This view is supported by the fact that partially propagating nature is restored as we increase the systems size to $N = 50$ for this value of $\dot{\epsilon}_a$.

Having explained the origin of the two-slope nature of the Lyapunov dimension D_L as a function of the system size N in the region of $\dot{\epsilon}_a$ where partially propagative bands are seen, we need to rationalize the linear dependence of D_L versus N both for low $\dot{\epsilon}_a$, where uncorrelated bands are seen, and for high $\dot{\epsilon}_a$, where fully propagative bands are seen. We have examined the space-time plots for various system sizes for low and high $\dot{\epsilon}_a$. In both these cases, the basic character of the spatial patterns is not altered when the system size is small. For instance, for small $\dot{\epsilon}_a$, the burstlike character of ρ_m is not altered when N values are small. Similarly, for $\dot{\epsilon}_a$ values corresponding to the fully propagative regime, say, $\dot{\epsilon}_a = 240$, choosing a small system size retains the propagative character. A space-time plot for $\dot{\epsilon}_a = 240$ and $N = 20$ shows this feature in Fig. 11(a). Indeed, one difference between this and the spatial pattern for $N = 100$ is that the band is reflected several times [compare Fig. 5(a)]. Due to the propagative nature, only small-amplitude serrations are seen as in the case of large system sizes. However, the stress serration amplitude and frequency are larger than that for an equivalent system $N = 100$ shown in Fig. 5(b).

Since the dependence of n_λ^+ and H on the system size is less pronounced due to a small number of positive exponents, we will not discuss this point.

We have also calculated the distribution of Lyapunov exponents $D(\lambda)$ for the entire range of the instability domain. The distribution evolves with the applied strain rate. The changes in the distribution of Lyapunov exponents with $\dot{\epsilon}_a$ are illustrated using typical plots in the regimes of strain rates corresponding to the randomly nucleated bands, the partially propagating bands, and the fully propagating bands, respectively. (These results are for $N = 100$, but the results hold for system sizes up to $N = 150$ examined. We note that $N > 150$ system sizes have not been studied due to the high computing time required for each run and the range of values of $\dot{\epsilon}_a$ investigated.) The evolution of the distribution with respect to $\dot{\epsilon}_a$ is shown in Figs. 12(a)–12(c). As can be seen from the figures, in general, $D(\lambda)$ is bimodal with peaks around zero and -0.08. At low strain rates corresponding to the randomly nucleated bands ($\dot{\epsilon}_a = 40$), the peak at -0.08 is strongly skewed to right, while that at zero is less skewed. The region between these two peaks has no exponents. As we increase $\dot{\epsilon}_a$, the peaks spread out, reducing the skewness of the bimodal distribution. A typical plot of $D(\lambda)$ for $\dot{\epsilon}_a = 90$ corresponding to the early stages of the partially propagating

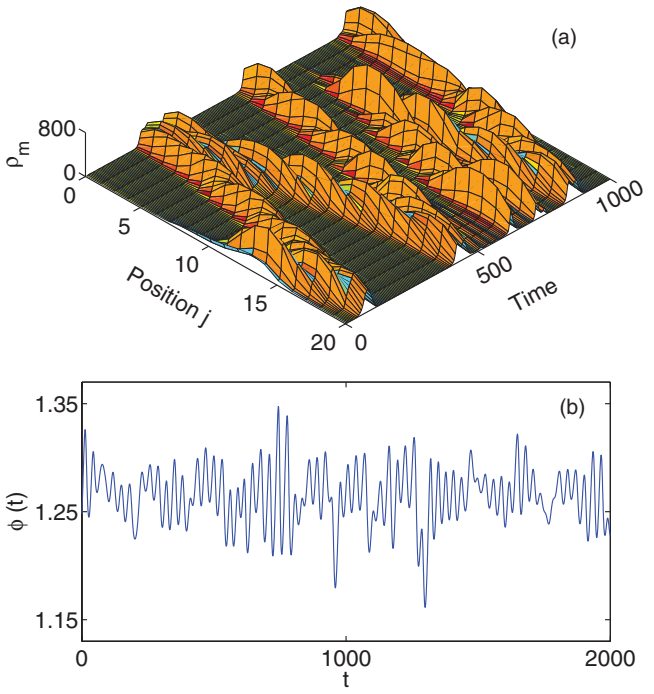

FIG. 11. (Color online) (a) Space-time plot of the mobile dislocation density for $N = 20$ and $\dot{\epsilon}_a = 240$ corresponding to the fully propagative band. (b) The corresponding stress-time plot.

band regime is shown in Fig. 12(b). As we increase the applied strain rate further, the two peaks at zero and -0.08 of $D(\lambda)$ spread out even more to fill the gap between the peaks. These features are illustrated in Fig. 12(c), where a plot of $D(\lambda)$ for $\dot{\epsilon}_a = 280$ corresponding to the fully propagative regime is shown. It should be mentioned here that the fully propagating bands are seen for values of $\dot{\epsilon}_a$ beyond 240.

VI. DYNAMICAL ANALYSIS OF STRESS SIGNALS

As discussed in the previous section, the stress signals from the model are irregular in the entire interval of the instability. Furthermore, the nature of stress serrations changes with the applied strain rate and is correlated with the extent of propagation of the dislocation band. In our earlier work, we demonstrated unambiguously that the irregular stress signals at low strain rates ($\dot{\epsilon}_a < 50$) are low-dimensionally chaotic [29]. However, no effort was made to quantify these stress signals in the region of strain rates where partially propagating to fully propagative bands are seen. This is undertaken in this section. For this purpose, we use a slightly modified algorithm for analyzing spatiotemporal chaotic systems [41,42]. In addition, the results of the previous section on the altered spatiotemporal patterns from the partially propagative nature (for large N) to the burst type for small system sizes raises the question of whether these stress signals also project low-d chaos. We will also address this question by using the same algorithm that was used in I [29].

We begin by briefly recapitulating the algorithm used in our earlier work [29]. The standard Grassberger-Procaccia (GP) algorithm involves reconstructing the attractor using delay

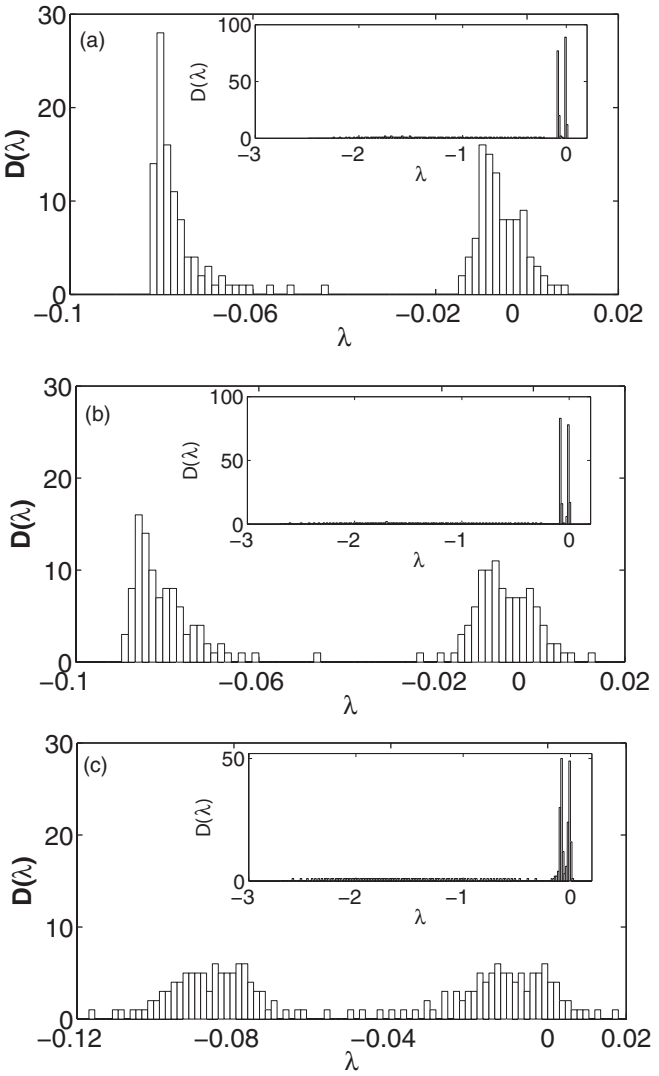

FIG. 12. Distribution of Lyapunov exponents for $N = 100$ and $\dot{\epsilon}_a = 40$ (a), 90 (b), and 280 (c). The inset shows the distribution over the entire range.

embedding technique [26,43–45]. Given a stress-time series defined by $\{\phi(k), k = 1,2,\ldots,M\}$, where k is in units of δt and M is the number of data points, the d-dimensional vectors are defined by $\vec{\xi}_k = \{\phi(k),\phi(k+\tau),\ldots,\phi[k+(d_E-1)\tau]\}$; $k = 1,2,\ldots,[M-(d_E-1)\tau]$, where τ is the delay time and d_E is the embedding dimension. The correlation integral defined as the fraction of the pairs of points $\vec{\xi}_i$ and $\vec{\xi}_j$ whose distance is less than a specified value r is given by

$$C(r,d_E) = \frac{1}{N_p}\sum_{i,j}\Theta(r - |\vec{\xi}_i - \vec{\xi}_j|), \tag{5}$$

where $\Theta(\cdots)$ is the step function and N_p is the number of vector pairs used in the sum [44]. If the attractor is self-similar, the correlation dimension is given by

$$D_2 = \lim_{r\to 0}\lim_{d\to\infty}\frac{\ln C(r,d_E)}{\ln r} \tag{6}$$

if the limit exists. In practice, however, the slope $D_2(r,d_E) = d\ln C(r,d_E)/d\ln r$ converges to a finite value D_2 for some

intermediate length scales. The improved method used in our earlier work combines several improvements suggested in the literature for making the conventional GP algorithm more effective. For instance, we use an optimum value of $(d_E - 1)\tau$ that maximizes the scaling regime [46]. Further, to enhance the scaling region at the upper end of the scale, we compensate for the finite size of the attractor by normalizing the local slope $D_2(r,d_E)$ of the attractor by half the local slope of the attractor in two dimensions $D_2(r,2)/2$. (See for details Ref. [29].) Thus we use following expression for the correlation dimension:

$$D_{2s}(r,d_E) = \frac{2d\ln C_2(r,d_E)}{d\ln C_2(r,2)}, \tag{7}$$

where $C_2(r,2)^{1/2}$ has been used in place of $C_{2r}(r,d_E)$, corresponding to an equivalent random attractor, as was done in Ref. [41]. When $D_{2s}(r,d_E)$ remains constant over a fair range of $\ln r$, it is taken to represent the correlation dimension D_2. The choice of $C_2(r,2)^{1/2}$ is motivated by the fact that any dimension less than the true dimension of the attractor gives essentially a uniform distribution and thus using $C_2(r,2)^{1/2}$ would not only serve to correct for the edge effects of the attractor as does $C_{2r}(r,d_E)$, but it would also take into account the contribution arising from finite delay time. The delay time used is the value of τ for which the slopes $D_2(r,2)$ converge for large scales (see [47]).

When the slope $D_{2s}(r,d_E)$ keeps increasing with the embedding dimension as found for stress signals in the partially to fully propagative band regime of $\dot{\epsilon}_a$, or when there is a lack of appreciable scaling regime for $D_{2s}(r,d_E)$, it might suggest a more complex dynamics that might reflect the spatially extended nature of the full system. In such cases it would be more appropriate to calculate the correlation dimensional density $\rho_{2s}(r,d_E)$. [Most calculations in the literature that estimate $\rho_{2s}(r,d_E)$ have been carried out for coupled map lattices.] For extensive chaos, Bauer *et al.* [41] suggest normalization using the equivalent random attractor for which $D_{2r} = \frac{d\ln C_{2r}(r,d_E)}{d\ln r}$ is expected to scale with d_E. Here $C_{2r}(r,d_E)$ is the correlation integral of an equivalent random attractor [41]. Then the correlation density is given by Ref. [41]

$$\rho_{2s}(r,d_E) = \frac{1}{d_E}\frac{D_2(r,d_E)}{D_{2r}(r,d_E)} = \frac{1}{d_E}\frac{d\ln C_2(r,d_E)}{d\ln C_{2r}(r,d_E)}. \tag{8}$$

Another prescription suggested is to compensate for the edge effects by normalizing $D_2^n(r,d_E)$ corresponding to near-neighbor vectors with respect to that corresponding to well separated vectors [42]. However, in our work we use $D_2(r,2)/2$ for normalization and thus the corresponding correlation density is given by

$$\rho_{2s}(r,d_E) = \frac{D_{2s}(r,d_E)}{d_E} = \frac{2}{d_E}\frac{d\ln C_2(r,d_E)}{d\ln C_2(r,2)}. \tag{9}$$

When $\rho_{2s}(r,d_E)$ remains constant for at least two orders in $\ln r$, it is taken to represent the correlation dimension density. We note that the scaling regime is always found at large scales due to the inevitable limited data and the high embedding dimensions required to obtain the scaling regime. For this reason, it is also referred to as a large-scale dimension density [42]. For the spatiotemporal chaotic systems (studied mostly using coupled map lattices), the scaling region is typically found at large length scales from half the attractor size down to a length scale where there is a sufficient number of points for such high embedding dimensions used. For this reason, the constant slope, though seen essentially at large scales (compared to low-dimensional chaos), is taken to be representative of the correlation dimension density ρ_2. (For instance, the scaling regime is found to be $-3.5 \leqslant \log_2 r \leqslant -0.8$ in studies on coupled lattice maps [41].) We shall also adopt the same convention.

In the present problem, we are faced with an additional complication of having to obtain the stress-time series by solving $3N + 1$ sets of equations. This is very demanding in terms of computational time when the number of sites N is large. It is compounded by the fact that our study requires that we scan a range of values of the drive parameter $\dot{\epsilon}_a$ and N. For this reason, we use $N = 100$. The maximum length of the time series used for our calculations was 1.1×10^5 time steps of $\Delta t = 0.5$ after discarding initial 20 000 points.

A. Results

As shown in I [29], the algorithm outlined above for calculating D_2 [Eq. (7)] works very well even for short time series for low-d attractors such as the the Lorenz model as well as for higher-dimensional attractors such as the sum of two Lorenz time series. Here we first verify if our earlier result that low-d chaos is projected as long as there is a one-to-one correspondence between the bursts of mobile density and the stress drops is correct. For this, we use the stress signals from a small system size $N = 20$, keeping $\dot{\epsilon}_a = 120$. The small system size altered the spatiotemporal pattern from one of partially propagating band type for $N = 100$ to one of isolated dislocation band type. A plot of $D_{2s}(r,d_E)$ is shown in Fig. 13(a), where we have used $(d_E - 1)\tau = 24$. The normalization used is with respect to $D_2(r,2)/2$ for $\tau = 15$. [The value of the τ used for the normalization of $D_2(r,2)$ is that value of τ leading to converged values of $D_2(r,2)$ for large scales.] It is clear that there is nearly five orders of scaling regime. The value of D_2 is $\sim$2.1, which is the same as that for large system size and low $\dot{\epsilon}_a$ ($\leqslant$50). For the sake of comparison, we have also plotted $D_{2s}(r,d_E)$ in Fig. 13(b) for $N = 100$ and $\dot{\epsilon}_a = 40$ [$(d_E - 1)\tau = 36$ where the normalization is with respect to $D_2(r,2)/2$ for $\tau = 24$]. It is clear that the scaling region for $N = 100$ size [Fig. 13(b)] is slightly larger than that for $N = 20$ shown in Fig. 13(a). The shorter scaling region in Fig. 13(a) can be attributed to the bursts of ρ_m occurring at the boundaries. [See Fig. 10(a).] This confirms our assertion that low-d chaos is projected whenever the stated correspondence between isolated bursts of ρ_m and stress drops holds.

As shown earlier, for higher values of $\dot{\epsilon}_a$, say, 90, $D_{2s}(r,d_E)$ keeps increasing without saturating for smaller scales until fluctuations take over as was shown in I [29] (see Fig. 8(b) of I [29]). A similar trend is seen for the entire range of values of $\dot{\epsilon}_a$ in the partially propagative band regime. Since the stress signals remain irregular, it is possible that the stress-strain time series reflect the spatiotemporal chaotic nature of the full system. Thus we consider evaluating dimensional density $\rho_{2s}(r,d_E)$ using Eq. (9) by embedding the stress-time series in successively higher dimensions. The length of the time series used is 1.1×10^5. The results presented in Fig. 14 are for $\dot{\epsilon}_a = 150$, for which there is considerable band propagation.

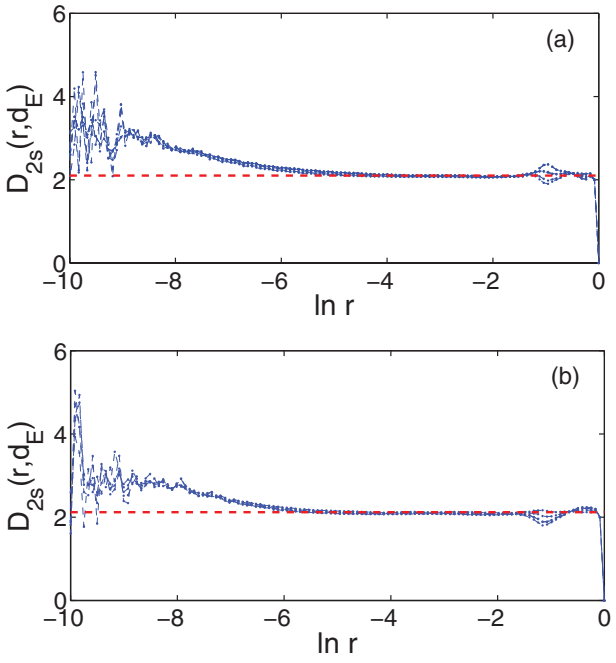

FIG. 13. (Color online) (a) Plot of $D_{2s}(r,d_E)$ as a function of $\ln r$ for $N = 20$ and $\dot{\epsilon}_a = 120$; $(d_E - 1)\tau = 24$ and the normalization used is $D_2(r,2)/2$ for $\tau = 15$. (b) Plot of $D_{2s}(r,d_E)$ as a function of $\ln r$ for $N = 100$ and $\dot{\epsilon}_a = 40$; $(d_E - 1)\tau = 36$ and the normalization used is $D_2(r,2)/2$ for $\tau = 24$.

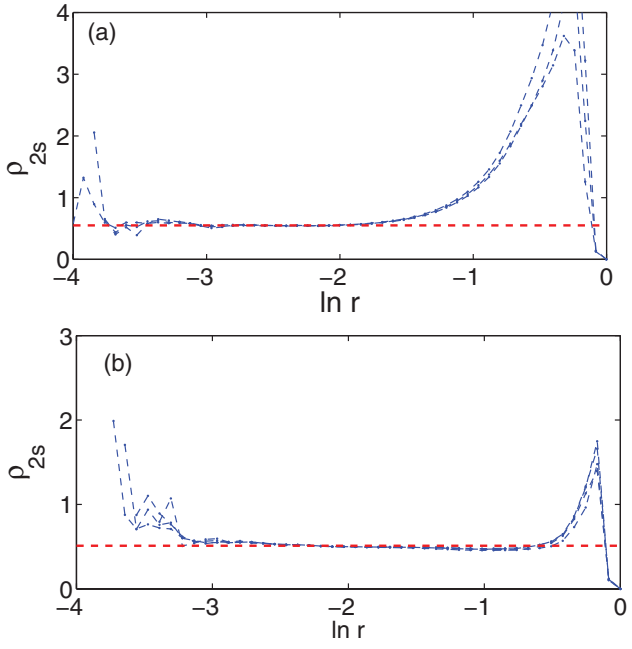

FIG. 14. (Color online) (a) Dimensional density for $\dot{\epsilon}_a = 150$ for embedding dimension $d_E = 14$–16, keeping $\tau = 12$. The normalization used is $D_2(r,2)$ for $\tau = 25$. The horizontal (red) dashed line is a guide for the eye and the value of $\rho_2 = 0.55$. A two orders of scaling region from $\ln r = -3.75$ to -1.7 is clear. (b) Dimensional density for $\dot{\epsilon}_a = 240$ for embedding dimension $d_E = 17$–20, keeping $\tau = 11$. The normalization used is $D_2(r,2)$ for $\tau = 22$. The horizontal (red) dashed line is a guide for the eye and the value of $\rho_2 = 0.51$. A nearly three orders of scaling region from $\ln r = -3.25$ to -0.5 is clear.

The delay time used for $D_{2s}(r,d_E)$ is $\tau = 12$. [The value of τ used is 24 for the normalization factor $D_2(r,2)/2$.] For clarity, we have presented plots of $\rho_{2s}(r,d_E)$ as a function of $\ln r$ for $d_E = 13$–15 in Fig. 14. One can clearly see a scaling regime of $-3.75 \leqslant \ln r \leqslant -1.7$, which is nearly two orders scaling regime. (This roughly corresponds to three orders in $\log_2$ base.) The value of $\rho_2 \sim 0.55 \pm 0.02$. The extent of the scaling regime in our case is *better* than that reported by Bauer *et al.* [41] and that reported in Ref. [42]. [See Fig. 1(b) of Ref. [41], where the scaling regime is about one and half orders in $\log_2$ base for coupled map lattices and two and a half orders of scaling in $\log_2$ base in Ref. [42].] We have also calculated the dimensional density $\rho_{2s}(r,d_E)$ for several values of strain rates $\dot{\epsilon}_a$ in the range 60–240. The range includes the fully propagating bands for $\dot{\epsilon}_a = 240$. A plot showing a nearly three orders of scaling regime in $\log_e$ base for ρ_{2s} is shown in Fig. 14(b) for $d_E = 17$–20 and $\dot{\epsilon}_a = 240$. In each case, we find a scaling regime that spans two to three orders. In this sense, our estimates of ρ_2 have a better confidence level than those in Refs. [41,42]. However, the dependence of the value of $\rho_{2s}(r,d_E)$ on $\dot{\epsilon}_a$ does not show any particular trend. The value of ρ_2 increases from 0.515 ± 0.01 for $\dot{\epsilon}_a = 120$ to 0.55 ± 0.02 for $\dot{\epsilon}_a = 150$ and then decreases to 0.51 ± 0.017 for $\dot{\epsilon}_a = 240$ corresponding to the region of fully propagating bands. On the basis of this, we conclude that the stress-time series corresponding to the partially propagative region to fully propagative band regime of strain rates exhibits features of extensive chaos.

VII. SUMMARY, DISCUSSION AND CONCLUSIONS

The focus of this paper was to examine what kind of information about the internal degrees of freedom is contained in the irregular scalar stress signals. Since the stress signal is a dynamical variable that determines the time evolution of the mobile dislocation density even as it is directly related to the spatial average over dislocation activity in the entire sample, our first task was to elucidate the connection between the spatiotemporal patterns and the nature of the irregularity of the stress signals. In our earlier work [29], we had demonstrated the one-to-one correspondence between the stress drops and the uncorrelated band types seen at low strain rates [29]. However, this correspondence breaks down in the region of partial propagation. For instance, even a small extent of propagation of the dislocation bands observed at $\dot{\epsilon}_a = 60$ leads to the interruption of the sequence of large stress drops by small-amplitude stress drops. A further increase in $\dot{\epsilon}_a$ leads to the increased extent of propagation, which in turn introduces longer stretches of small-amplitude stress drops. For a further increase in $\dot{\epsilon}_a$, say, for $\dot{\epsilon}_a = 240$, fully propagating bands are seen where numerous small-amplitude stress drops with few large stress drops are seen. *In essence, our study shows that there is a direct correlation between the temporal extent of small-amplitude serrations and the spatial extent of propagation.*

Better insight into the different types of bands can be obtained by noting that there are two length scales in our problem, namely, the mean burst size of the dislocation bands l_b and the (mean) propagation length l_p apart from the system size N. Both are functions of $\dot{\epsilon}_a$. If the propagation length

scale l_p is larger than N, then one sees the fully propagating bands. In contrast, if $l_p < N$, there are two possibilities. When $l_p < N$ but comparable and $l_p \gg l_b$, one sees the partially propagating bands; when l_p is comparable to but larger than l_b, a burst-type dynamics is seen. (Note that l_b is typically ∼10–15.) This case was studied by taking $N = 20$ and $\dot{\epsilon}_a = 120$ where we found isolated bursts of ρ_m for which $l_b \sim N$. However, the propagation length l_p increases with $\dot{\epsilon}_a$. At high strain rates, taking small N does not affect the fully propagating character of the bands. Indeed, we have investigated the effect of small system size on the spatial patterns in the fully propagating regime. We showed that for small system sizes (for example, $N = 20$) and high $\dot{\epsilon}_a$ (say, 240), the extent of propagation is increased in the sense that the band gets reflected at the boundaries several times, as is clear from Fig. 11. The amplitude and frequency of the associated stress signal are larger than those for $N = 100$. Our analysis also shows that the nature of the patterns evolves continuously due to the dependence of the two length scales l_b and l_p on the applied strain rate. *Thus the changes in the nature of band types are not associated with any bifurcation*.

Our earlier work demonstrated that a characteristic feature of the small-amplitude stress drops in the propagative band regime is that they follow a scale-free power law distribution [1,35], an indication of high-dimensional dynamics. Since small-amplitude stress drops also dominate at intermediate values of $\dot{\epsilon}_a$ corresponding to the partially propagating bands, it might suggest the possibility of a high-dimensional attractor for this range of strain rates as well. Indeed, it is in this regime of partially to fully propagating bands that we find a finite correlation dimension density in the stress signals with $\rho_2 \sim$ 0.51–0.55. We find two to three orders of scaling in $\log_e r$, which is better in extent than those reported in the studies of coupled map lattices [41,42]. Note that the breakdown of the scaling regime for smaller scales has more to do with the poor statistics (as in the low-d chaotic attractors), i.e., very few points are present at length scales lower than $\ln r < -4.0$ in such high embedding dimensions. Furthermore, the finite correlation dimension density obtained from stress-time series analysis demonstrates that the scalar stress signal does contain information about the extensive nature of the spatiotemporal chaotic dynamics of the internal degrees of freedom, which can be detected by an appropriate algorithm.

Although, we are primarily interested in characterizing the stress signals in the region of strain rates where partially propagating to fully propagating bands are seen, the altered dynamics from the partially propagating band type for large N [see Fig. 10(a)] to the burst type bands for small system sizes ($N = 20$, for example) gives us an opportunity to reconfirm our earlier result that low-d chaos is projected as long as there is a one-to-one correspondence between bursts of the mobile dislocation density and stress drops [29]. We find a more than four orders scaling regime for D_2 giving a well converged value of $D_2 \sim 2.1$, which is slightly less than that seen for $N = 100$ and $\dot{\epsilon}_a = 40$. This difference can be seen to be due to the presence of bursts in ρ_m at the boundaries.

The Lyapunov spectrum of the model equations has been calculated for the entire instability domain. The Lyapunov dimension scales with N only for small strain rates (isolated burst regime) and at high strain rates (fully propagating band regime). However, for intermediate $\dot{\epsilon}_a$ values where the partially propagating bands are seen, the Lyapunov dimension $D_L(N)$ exhibits two distinct slopes as a function of N (see Fig. 9). The larger slope in the D_L versus N plot seen for small system sizes has been traced to the influence of the boundary that alters the nature of spatiotemporal dynamics from one of the partially propagating bands to one of well separated bursts of ρ_m, a characteristic feature that is seen for low $\dot{\epsilon}_a < 60$ (and large N). The smaller slope in the D_L versus N plot is representative of a large system size. For large N, the Lyapunov density $\rho_L = D_L/N$ ranges from 0.32 to 0.38 for the entire instability domain of strain rates. Thus, in essence, the model equations are spatiotemporally chaotic.

However, the calculated values of the correlation dimension densities $\rho_2 \sim 0.51$–0.55 are larger than the values of Lyapunov density $\rho_L = D_L/N$, which ranges from 0.32 to 0.38 for large system sizes (in the regime of partially to the fully propagating bands regime of $\dot{\epsilon}_a$). Instead, we should have expected that ρ_L obtained from the full set of equations is larger than ρ_2 obtained from the stress signals. Indeed, this relation does hold for small system sizes, but not for large N. In contrast, our detailed study of the model demonstrates that the nature of spatiotemporal patterns changes when the system is small, which is the basic reason for the two-slope nature of $D_L(N)$. This may imply that under the conditions when the spatiotemporal patterns are sensitive to the system size, the inequality $\rho_L \geqslant \rho_2$ may not hold. We will revert to this point soon.

The discussion about the relationship between the nature of the band types and the Lyapunov density raises the following question: Should we not see the influence of system size on the correlation dimension density? This question cannot be addressed in the case of the partially propagating band types since the small system size alters the dynamics drastically from the fully propagating type to the isolated band type and the corresponding stress signal has a low-d character. However, this can be addressed in the region of high $\dot{\epsilon}_a$ where the spatiotemporal patterns remain in the fully propagating class even when N is reduced, but the stress-time curves are slightly altered with respect to the mean amplitude and the mean frequency, being more for low N values. To understand this question, we have calculated the correlation dimension density using stress signals from $N = 20, 40, 60$, and 80, keeping $\dot{\epsilon}_a = 240$ in the regime of fully propagating bands. Plots of ρ_{2s} for $N = 20$ and 40 are shown in Figs. 15(a) and 15(b), respectively. It is clear from the figures that the scaling region $-4.75 \leqslant \ln r \leqslant -0.85$ is about four orders for $N = 20$. The value of $\rho_2 \sim 0.3 \pm 0.01$ is much smaller than that for $N = 100$ for which $\rho_2 \sim 0.51 \pm 0.017$ [see Fig. 14(b)]. The correlation dimension density ρ_2 increases to 0.365 ± 0.01 as we increase N to 40 (with a slightly smaller scaling regime $-4.2 \leqslant \ln r \leqslant -0.85$) as can be seen from Fig. 15(b). As we increase N further, the value of ρ_2 reaches the large N limit of 0.51 for $N = 100$. *Thus, indeed, the system size does affect the value of the correlation dimension density as well*. Here it is worth noting that part of the reason for the larger scaling regime for $N = 20$ and $\dot{\epsilon}_a = 240$ compared to that for $N = 100$ is the lower value of ρ_2 that improves the statistics at lower length scales.

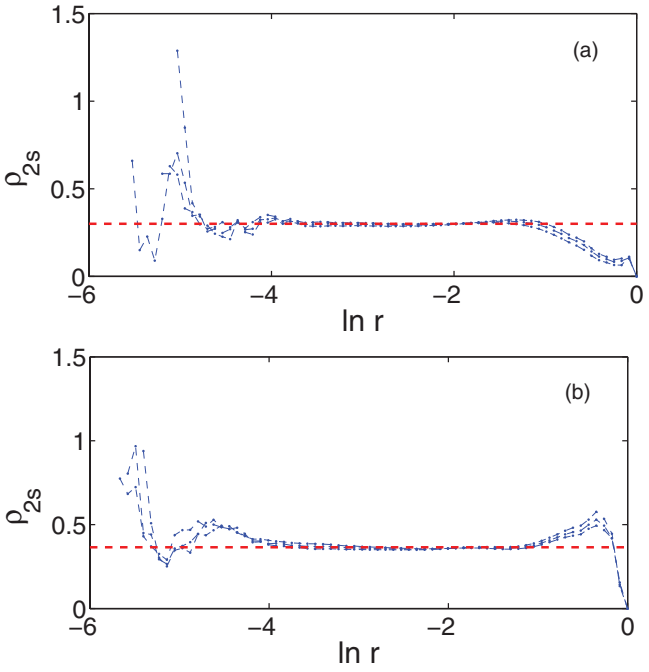

FIG. 15. (Color online) (a) Correlation dimensional density ρ_{2s} for $\dot{\epsilon}_a = 240$ for a small system size $N = 20$. The embedding dimensions used for the stress signals are $d_E = 18$–20, keeping $\tau = 8$. The normalization used is $D_2(r,2)$ for $\tau = 25$. The horizontal (red) dashed line is a guide for the eye and the value of $\rho_2 = 0.30$. A four orders of scaling region from $\ln r = -4.75$ to -0.85 is clear. (b) Correlation dimensional density for $\dot{\epsilon}_a = 240$ for a small system size $N = 40$. The embedding dimensions used for the stress signals are $d_E = 13$–15, keeping $\tau = 7$. The normalization used is $D_2(r,2)$ for $\tau = 19$. The horizontal (red) dashed line is a guide for the eye and the value of $\rho_2 = 0.365$. A three orders of scaling region from $\ln r = -4.2$ to -0.85 is clear.

One question that needs to be answered is whether the scaling regime found at large length scales for the correlation dimension density would continue to smaller length scales when the length of the time series is increased. While it is difficult to verify this proposition due to the computational difficulties in handling long time series in such high embedding dimensions, the present results appear to support this possibility. (Any detectable change in the scaling region requires increasing the length of the time series by at least a factor of 10.) In contrast, a decrease in the magnitude of the correlation dimension density affords an easier way to check this statement. This is what we see when we analyze the time series corresponding to a small system size, keeping the applied strain rate at a value corresponding to the fully propagating band. In this case, the value of the correlation dimension density decreases from $\rho_2 \sim 0.51$ to 0.3, which is clearly responsible for the scaling regime extending to scales less than $-\ln 4$. This length scale is even comparable to the lower limit of scaling ($-\ln 5.5$) found in the case of the sum of two independent x components of the Lorenz model (see Fig. 6 of Ref. [29]).

Having recognized that both the correlation density and Lyapunov dimension depend on the system size, it would be interesting to estimate the extent to which a finite system size contributes to ρ_L. Clearly, this issue cannot be addressed for small systems sizes $N < N_{\min}$ since the nature of the spatiotemporal patterns is drastically altered. Furthermore, even for the fully propagating regime, we have just demonstrated that $\rho_2 \sim 0.365$ for $N = 40$, which is smaller than $\rho_L \sim 0.37$. Thus this issue cannot be addressed for small N. The simplest case for estimating the effective ρ_L^{eff} is the large N case of the fully propagating bands for which $\rho_L = D_L/N = 0.37$. We first note that the stress-time series used for the time series analysis is for a system size $N = 100$. Since stress is determined by the spatial average of dislocation activity in the entire sample, it would contain effects arising from the influence of the boundary due to the finite width of burst of ρ_m. The effective system size N_{eff} can be taken to $N_{\text{eff}} = N - 2l_b$. The value of l_b for the propagating band is typically 15. Using this, we find $\rho_L^{\text{eff}} \sim 0.528$, which is larger than $\rho_2 \sim 0.51$ for this value of strain rate. Thus it appears that the effective Lyapunov dimension density is larger than the correlation dimension density ρ_2 (0.51). However, a similar exercise for the region of strain rates corresponding to the partially propagating bands is less straightforward since D_L versus N exhibits two slopes. Assuming that the mean slope of the D_L versus N plot is a reasonable choice for the slope of a large systems size, we have estimated ρ_L^{eff}. We find that for the entire interval of partially propagating bands (and using the effective system size N_{eff} as earlier) ρ_L^{eff} is always larger than ρ_2 obtained from the time series analysis.

A few comments are in order regarding the Lyapunov dimension. A standard way to calculate the Lyapunov spectrum of spatiotemporal chaotic systems is to use increasing subsystem sizes and extrapolate it as a function of system size [48,49]. However, the method assumes that the subsystem dynamics is not altered when the size of the subsystem is increased. This method cannot be followed in our case as the nature of the spatiotemporal dynamics is affected even when the system size is not too small, say, $N = 40$ for the midrange of $\dot{\epsilon}_a$. At best the method works when the system size is large enough that the spatiotemporal patterns are not affected. Then the utility of the method is lost. At a technical level, this method is not meaningful for our model since the variation of the stress rate equation [Eq. (4)] contains contributions arising from all the variables defined at all sites. Thus, using the truncated Jacobian of the subsystem would introduce considerable error if we leave out the contribution arising from the entire set of sites of the full system.

It is useful to contrast our results with the earlier studies on the spatiotemporal dynamics of spatially extended systems. Most studies on the calculation of the correlation dimension density for spatiotemporal chaotic systems are based on coupled map lattices. These studies use vectors constructed from n site variables [41,42]. However, we are not aware of a time series analysis carried out using a scalar signal derived from some kind of spatial average of site variables.

In the AK model, stress is not some artificially generated spatial average, but is a dynamical variable that couples to other variables. Specifically, while the stress at a given time is determined by the spatial average over the dislocation activity in the entire sample, the subsequent growth or decay of $\rho_m(x,t)$ (and hence other densities) at the next moment is itself determined by its current value of the

stress. In this sense, the system could be a special system where the dynamical invariants depend on the system size.

The surprising result from our study is that low-d chaos is projected from the scalar stress signals even though the internal degrees of freedom exhibit spatiotemporal chaotic dynamics. Even though this result is obtained from the AK model, we believe that it should hold at least in situations where one can set up a one-to-one correspondence between the abrupt variation of a scalar time series and localized excitations of the internal degrees of freedom. Indeed, the altered spatiotemporal patterns from the partially propagating band type to burst type when N is taken to be small supports the result. Furthermore, projecting low-d chaos holds at least in one other case we have examined [22,23]. In our recent studies on the spatiotemporal dynamics of peeling of adhesive tape, we represented the acoustic energy dissipated as the spatial average of local strain rates of the peel front [22,23]. These studies show that the model equations are spatiotemporally chaotic while the AE signals are low-d chaotic. Furthermore, a simple spatial average over the variable defined on all spatial elements may show low-d chaos in contrast to the AK model where stress is a dynamical variable. This also suggests that the nature of a spatial average may not be relevant for the study since there is no feedback to other variables as in the AK model equations.

ACKNOWLEDGMENTS

G.A. acknowledges the Board of Research in Nuclear Sciences (BRNS) Grants No. 2007/36/62 and No. 2012/36/18 and support from the Indian National Science Academy through a Senior Scientist Position. R.S. acknowledges support from the BRNS Grants.

[1] G. Ananthakrishna, Phys. Rep. **440**, 113 (2007).
[2] M. Zaiser, Adv. Phys. **55**, 185 (2006).
[3] R. M. Fisher and J. S. Lally, Can. J. Phys. **45**, 1147 (1967); H. Dunegan and D. Harris, Ultrasonics **7**, 160 (1969); D. R. James and S. H. Carpenter, J. Appl. Phys. **42**, 4685 (1971).
[4] D. M. Dimiduk, C. Woodward, R. Le Sar, and M. D. Uchic, Science **312**, 1188 (2006).
[5] E. M. Nadgorny, J. Mater. Res. **23**, 2829 (2008).
[6] K. S. Ng and A. H. W. Ngan, Acta Mater. **56**, 1712 (2008).
[7] M. Zaiser, J. Schwerdtfeger, A. S. Schneider, C. P. Frick, B. G. Clark, P. A. Gruber, and S. Arzt, Philos. Mag. **88**, 30 (2008).
[8] B. Devincre, T. Hok, and L. Kubin, Science **320**, 1745 (2008).
[9] F. F. Csikor *et al.*, Science **318**, 251 (2007).
[10] A. detailed study of this effect is due to F. Le Chatelier, Rev. Métall. **6**, 914 (1909); however, the phenomenon was first observed by F. Savart, Ann. Chim. Phys. Ser. 2 **65**, 337 (1837).
[11] A. H. Cottrell, *Dislocations and Plastic Flow in Crystals* (Oxford University Press, Oxford, 1953).
[12] H. Neuhäusser, in *Dislocations in Solids*, edited by F. R. N. Nabarro, Vol. 6 (North-Holland, Amsterdam, 1983).
[13] M. A. Lebyodkin and Y. Estrin, Acta. Mater. **53**, 3403 (2005); M. A. Lebyodkin and T. A. Lebedkina, Phys. Rev. E **77**, 026111 (2008).
[14] J. Kumar and G. Ananthakrishna, Phys. Rev. Lett. **106**, 106001 (2011).
[15] S. J. Noronha, G. Ananthakrishna, L. Quaouire, C. Fressengeas, and L. P. Kubin, Int. J. Bifurcat. Chaos **7**, 2577 (1997).
[16] G. Ananthakrishna, S. J. Noronha, C. Fressengeas, and L. P. Kubin, Phys. Rev. E **60**, 5455 (1999).
[17] M. S. Bharathi, M. Lebyodkin, G. Ananthakrishna, C. Fressengeas, and L. P. Kubin, Phys. Rev. Lett. **87**, 165508 (2001).
[18] M. S. Bharathi, M. Lebyodkin, G. Ananthakrishna, C. Fressengeas, and L. P. Kubin, Acta Mater. **50**, 2813 (2002).
[19] D. Maugis and M. Barquins, in *Adhesion*, edited by K. W. Allen, Vol. 12 (Elsevier, London, 1988).
[20] M. Ciccotti, B. Giorgini, D. Villet, and M. Barquins, Int. J. Adhes. **24**, 143 (2004).
[21] R. De and G. Ananthakrishna, Phys. Rev. Lett. **97**, 165503 (2006).
[22] J. Kumar, M. Ciccotti, and G. Ananthakrishna, Phys. Rev. E **77**, 045202(R) (2008).
[23] J. Kumar, R. De, and G. Ananthakrishna, Phys. Rev. E **78**, 066119 (2008).
[24] Y. Urahama, J. Adhes. **31**, 47 (1989).
[25] Y. Yamazaki and A. Toda, Physica D **214**, 120 (2006).
[26] H. Kantz and T. Schriber, *Nonlinear Time Series Analysis* (Cambridge University Press, Cambridge, 1997).
[27] O. Peters and J. D. Neelin, Nat. Phys. **2**, 393 (2006).
[28] P. E. Dimotakis, H. J. Catrakis, and D. C. Fourguette, J. Fluid Mech. **433**, 105 (2001).
[29] R. Sarmah and G. Ananthakrishna, Phys. Rev. E **86**, 056208 (2012).
[30] A. Van den Beukel, Phys. Status Solidi A **30**, 197 (1975).
[31] L. P. Kubin and Y. Estrin, Acta. Metall. **33**, 397 (1985).
[32] P. Penning, Acta Metall. **20**, 1169 (1972).
[33] G. Ananthakrishna and M. C. Valsakumar, J. Phys. D **15**, L171 (1982).
[34] G. Ananthakrishna and M. C. Valsakumar, Phys. Lett. A **95**, 69 (1983).
[35] M. S. Bharathi and G. Ananthakrishna, Europhys. Lett. **60**, 234 (2002).
[36] M. S. Bharathi and G. Ananthakrishna, Phys. Rev. E **67**, 065104(R) (2003).
[37] M. S. Bharathi, S. Rajesh, and G. Ananthakrishna, Scr. Mater. **48**, 1355 (2003).
[38] G. Dee and J. S. Langer, Phys. Rev. Lett. **50**, 383 (1983).
[39] However, one notices the distinct nature of the upturns in the experimental signals compared to the rounded wave form of the model stress signals. This is due to the fact that the time scales of the plastic strain rate bursts (or, equivalently, the mobile density bursts) in experiments are significantly faster than those of the model plastic strain rate bursts (or ρ_m). Though it is possible to use much shorter time scales in our model, it poses serious difficulties for the extensive computations needed to obtain the kind of results presented here.

[40] G. Benettin, L. Galgani, A. Giorgilli, and J.-M. Strelcyn, Meccanica **15**, 9 (1980); **15**, 21 (1980).
[41] M. Bauer, H. Heng, and W. Martienssen, Phys. Rev. Lett. **71**, 521 (1993); H. Heng, M. Bauer, and W. Martienssen, Chaos Solitons Fractals **2**, 197 (1996).
[42] C. Raab and J. Kurths, Phys. Rev. E **64**, 016216 (2001).
[43] N. H. Packard, J. P. Crutchfield, J. D. Farmer, and R. S. Shaw, Phys. Rev. Lett. **45**, 712 (1980).
[44] P. Grassberger and I. Procaccia, Phys. Rev. Lett. **50**, 346 (1983); Physica D **9**, 189 (1983).
[45] M. Ding, C. Grebogi, E. Ott, T. Sauer, and J. A. Yorke, Phys. Rev. Lett. **70**, 3872 (1993).
[46] A. M. Albano, J. Muench, C. Schwartz, A. I. Mees, and P. E. Rapp, Phys. Rev. A **38**, 3017 (1988).
[47] E. Olbrich and H. Kantz, Phys. Lett. A **232**, 63 (1997).
[48] R. Carretero-González, S. Ørstavik, J. Huke, D. S. Broomhead, and J. Stark, Chaos **9**, 466 (1999).
[49] S. Ørstavik, R. Carretero-González, and J. Stark, Physica D **147**, 204 (2000).